Journal of Biomedical Optics

BiomedicalOptics.SPIEDigitalLibrary.org

Aberration correction method based on double-helix point spread function

Zhaojun Wang
Yanan Cai
Yansheng Liang
Dan Dan
Baoli Yao
Ming Lei

Zhaojun Wang, Yanan Cai, Yansheng Liang, Dan Dan, Baoli Yao, Ming Lei, "Aberration correction method based on double-helix point spread function," *J. Biomed. Opt.* **24**(3), 031005 (2018), doi: 10.1117/1.JBO.24.3.031005.

Journal of Biomedical Optics 24(3), 031005 (March 2019)

Aberration correction method based on double-helix point spread function

Zhaojun Wang,[a,b] Yanan Cai,[a,b] Yansheng Liang,[a,b] Dan Dan,[a,c] Baoli Yao,[a,c,*] and Ming Lei[a,c,*]
[a]Chinese Academy of Sciences, Xi'an Institute of Optics and Precision Mechanics, State Key Laboratory of Transient Optics and Photonics, No. 17 Xinxi Road, Xi'an, Shaanxi 710119, China
[b]University of Chinese Academy of Sciences, No. 19 Yuquan Road, Shijingshan District, Beijing 100049, China
[c]Xi'an Jiaotong University, No. 28 Xianning West Road, Xi'an, Shaanxi 710049, China

Abstract. Point spread function (PSF) engineering has met with lots of interest in various optical imaging techniques, including super-resolution microscopy, microparticle tracking, and extended depth-of-field microscopy. The intensity distributions of the modified PSFs often suffer from deteriorations caused by system aberrations, which greatly degrade the image contrast, resolution, or localization precision. We present an aberration correction method using a spiral-phase-based double-helix PSF as an aberration indicator, which is sensitive and quantitatively correlated to the spherical aberration, coma, and astigmatism. Superior to the routine iteration-based correction methods, the presented approach is iteration-free and the aberration coefficients can be directly calculated with the measured parameters, relieving the computing burden. The validity of the method is verified by both examining the intensity distribution of the conventional Gaussian PSF in three dimensions and observing muntjac skin fibroblast cells. This iteration-free correction method has a potential application in PSF engineering systems equipped with a spatial light modulator. [DOI: 10.1117/1.JBO.24.3.031005]

Keywords: aberration correction; double-helix point spread function; iteration-free.

Paper 180362SSR received Jun. 23, 2018; accepted for publication Aug. 16, 2018; published online Sep. 4, 2018.

1 Introduction

Point spread function (PSF) engineering has been a routine technique in various applications, such as super-resolution microscopy,[1] microparticle tracking,[2] and extended depth-of-field microscopy.[3,4] Apart from the conventional imaging systems, PSFs are regularly modified into a variety of shapes, including biplane PSF,[5] Bessel PSF,[6] cubic-phase PSF,[7,8] astigmatic PSF,[9] and double-helix PSF[10,11] (DH-PSF), by which improved imaging resolution, axial localization precision, or depth-of-field can be achieved. PSFs of imaging systems are often distorted by system aberrations, which stem from misaligned optical elements, surface-shape error of the optical components, and refractive-index mismatch.[12–15] As a consequence, imaging performance inevitably degrades, making aberration correction an essential procedure in these applications.

Generally, the premeasured aberration can be compensated by introducing a conjugated phase with adaptive optical elements, such as a spatial light modulator (SLM). Existing aberration measurement techniques can be categorized into direct wavefront sensing and indirect wavefront sensing.[16,17] Direct sensing is usually implemented with a Shack–Hartmann wavefront sensor,[18–21] which can provide high speed measurement; however, its requirement of both a wavefront sensor and a correction element increases the cost and complexity of the system.[17] In contrast, indirect sensing methods only require a wavefront correction element, which makes them more economical and convenient for the construction of microscopes.[22–25] Typically, images of fluorescent beads at different focusing depths are used to retrieve, the aberration, by transferring phases and amplitudes iteratively between the focal plane and the pupil plane.[22,26] However, the precision of the indirect sensing method is limited by the employed Gaussian PSF, due to its weak response to wavefront error. Superior to Gaussian PSF, optical vortices with symmetrical doughnut shapes are more sensitive to phase irregularity. Slight wavefront distortion will destroy its rotationally symmetric intensity distribution. For this reason, Jesacher et al.[27] utilized the doughnut PSF to determine the astigmatism caused by the flatness deviation of SLM; however, this approach was irresponsive for spherical aberration. In addition, the above indirect sensing methods are all modified from iteration-based algorithms, which are time-consuming and may not converge sometimes.[28–30]

To circumvent the above problems, we propose an iteration-free aberration correction method with high sensitivity by employing a newly proposed double-helix PSF[31,32] as the aberration indicator. Double-helix PSF is originally generated with the superposition of Gaussian–Laguerre (GL) modes,[33] which is proved to be of high efficiency and has become the mainstream generation method in related applications.[10,34,35] The influence of aberrations on the double-helix PSF has been characterized by former researchers.[36,37] Nevertheless, none of them reveal the potential of the double-helix PSF in aberration correction, because the shape of aberration-free double-helix PSF based on GL modes somehow deviates from the ideal double-helix shape, which makes it difficult to depict the distortions.[31] Recently, an approach to generating the double-helix PSF based on spiral phase[38] was developed and proved to be more efficient and flexible.[32] In Ref. 31, we employed this double-helix PSF to build a single-shot three-dimensional (3-D)

---

*Address all correspondence to: Ming Lei, E-mail: leiming@opt.ac.cn; Baoli Yao, E-mail: yaobl@opt.ac.cn

fluorescent microscope and surprisingly found that the double-helix PSF based on spiral phase is closer to an ideal double-helix shape for its uniform rotation rate and interlobe distance, with which the distortions of the PSF can be easily quantified. Therefore, in this paper, we further adopt the spiral-phase-based double-helix PSF as the indicator of aberrations. The proposed double-helix PSF is sensitive to not only the coma and the astigmatism, but also the spherical aberration.[31] Moreover, the coefficients of the aberrations can be directly calculated by analyzing the shape of measured double-helix PSFs without the iterative procedure, which relieves the computing burden and takes no convergence risk.

As a demonstration, we corrected the primary spherical aberration, primary x-coma, primary y-coma, primary 0-deg astigmatism, and primary 45-deg astigmatism of a high numerical aperture fluorescent microscope with the developed approach. The intensity distribution of the corrected 3-D Gaussian PSF was measured to be in good agreement with well-known aberration-free distribution. In addition, we also observed muntjac skin fibroblast cells with the identical system, of which the brightness and the image contrast were significantly improved after the correction. We anticipate that the iteration-free aberration correction method will have a potential application in PSF engineering systems.

2 Methods

The computer-generated holograms (CGH) to generate the spiral-phase-based double-helix PSF can be simply described by the equation below

$$P_N(\rho,\theta)=\begin{cases}(2n-1)\theta, & \sqrt{\frac{n-1}{N}}<\rho\le\sqrt{\frac{n}{N}}, n=1,2,\ldots,N\\ 0, & \rho>1\end{cases}, \tag{1}$$

where ρ represents the normalized radius of the selected aperture, $P_N(\rho,\theta)$ denotes the modulated phase at the polar coordinates (ρ,θ), and N is the total number of the Fresnel zones. The phase mask is composed of a sequence of radial sampling of the spiral phase into the Fresnel zones. The rotation rate and the interlobe distance of the PSF can be easily adjusted by changing the number of Fresnel zones.[31] Without loss of generality, we select N as 6 for all simulations.

The complex amplitude of the beam at the exit pupil plane is assumed to be

$$U_{\mathrm{ex}}(\rho,\theta)=E_{\mathrm{in}}(\rho,\theta,z=0)\exp\{i[P_N(\rho,\theta)+W(\rho,\theta)]\}, \tag{2}$$

where $E_{\mathrm{in}}(\rho,\theta,z=0)$ denotes the incident wave field distribution at the exit pupil plane, $P(\rho,\theta)$ represents the modulated phase to generate the double-helix PSF, and $W(\rho,\theta)$ is the wavefront aberration of the system. For simplicity, the incident wave is treated as uniform plane wave, i.e., let $E_{\mathrm{in}}(\rho,\theta,z=0)=1$. The propagation from the exit pupil plane to the observation plane is described by Fresnel–Kirchhoff diffraction theory, given as

$$U_{\mathrm{o}}(\rho',\theta',z)\propto\int_0^1\int_0^{2\pi}U_{\mathrm{ex}}(\rho,\theta)\exp\left(ik\frac{\rho^2}{2z}\right)\times\exp\left[-ik\frac{\rho\rho'\cos(\theta-\theta')}{z}\right]\rho\mathrm{d}\rho\,\mathrm{d}\theta, \tag{3}$$

where k represents the wave number and z is the distance between the two planes.

To keep consistent with the circular pupil of a routine optical system and the designed phase mask, we use Zernike circle polynomials to characterize the optical aberrations. For simplicity, we only consider primary spherical aberration, coma, and astigmatism here. Higher order aberrations can be analyzed in the same manner. Field curvature and distortion are out of our scope for they have no influence on the shape of the PSF.[39] Therefore, the wavefront aberration here can be described as

$$\begin{aligned}W(\rho,\theta)=\frac{2\pi}{\lambda}[&A_{\mathrm{s}}\bullet(6\rho^4-6\rho^2+1)\\&+A_{\mathrm{cx}}\bullet(3\rho^3-2\rho)\cos\theta+A_{\mathrm{cy}}\bullet(3\rho^3-2\rho)\sin\theta\\&+A_{\mathrm{ax}}\bullet\rho^2\cos 2\theta+A_{\mathrm{ay}}\bullet\rho^2\sin 2\theta],\end{aligned} \tag{4}$$

where A_{s}, A_{cx}, A_{cy}, A_{ax}, and A_{ay} are the corresponding coefficients of primary spherical aberration, primary x-coma, primary y-coma, primary 0-deg astigmatism, and primary 45-deg astigmatism in units of wavelength λ.

Figure 1 shows the double-helix PSFs affected by different types of aberrations. We can draw a sketchy conclusion that spherical aberration causes focal plane shift and generates a nonuniform rotation rate, coma unbalances the energy of the main lobes, and astigmatism brings about varying interlobe distances at different depths.[31] In fact, not only the spherical aberration but also the astigmatism affects the rotation rate. In addition, astigmatism and coma in different directions will affect the PSF in different ways, as shown in Figs. 1(c) and 1(d), respectively. In the following section, quantitative results will be presented in detail. We confine the coefficient of every single aberration within $0.6\,\lambda$.

2.1 *Quantitative Analysis of the Point Spread Function Deformation*

Figure 2 shows the quantitative deformation of the double-helix PSFs with varying spherical aberrations. To measure the rotation angle and the interlobe distance, positions where the two main lobes reach their maximum intensity are first obtained, which can be denoted as (x_1,y_1) and (x_2,y_2) (supposing $y_2>y_1$), respectively. Then, the rotation angle can be directly calculated as the angle deviation of the attachment of the two points from the y-axis, that is, $\arctan[(x_2-x_1)/(y_2-y_1)]$. Similarly, the interlobe distance can also be measured by calculating the distance of the two maximum points. As shown in Fig. 2(a), the focal plane where the rotation angle reaches 0-deg shifts with an increase in the spherical aberration, and the uniformity of the rotation rate is severely broken as A_{s} gets $>0.4\,\lambda$. Meanwhile, the interlobe distance gradually deviates from the nearly uniform curve with an increase in the spherical aberration [Fig. 2(b)]. Although the distorted interlobe distance curve cannot be approximated to a familiar function, its monotonicity could be helpful for the aberration correction, which will be discussed in Sec. 2.2.1. All deformations in the PSF become opposite as we choose an opposite A_{s}.

The quantitative deformation of the double-helix PSFs with varying 0-deg astigmatisms is shown in Figs. 3(a) and 3(b), respectively. Similarly, the focal plane shifts with the increasing 0-deg astigmatism and the rotation rate also turns into nonuniform. But the changing tendency is quite different. As the aberration coefficient increases, the rotation rate curve gradually

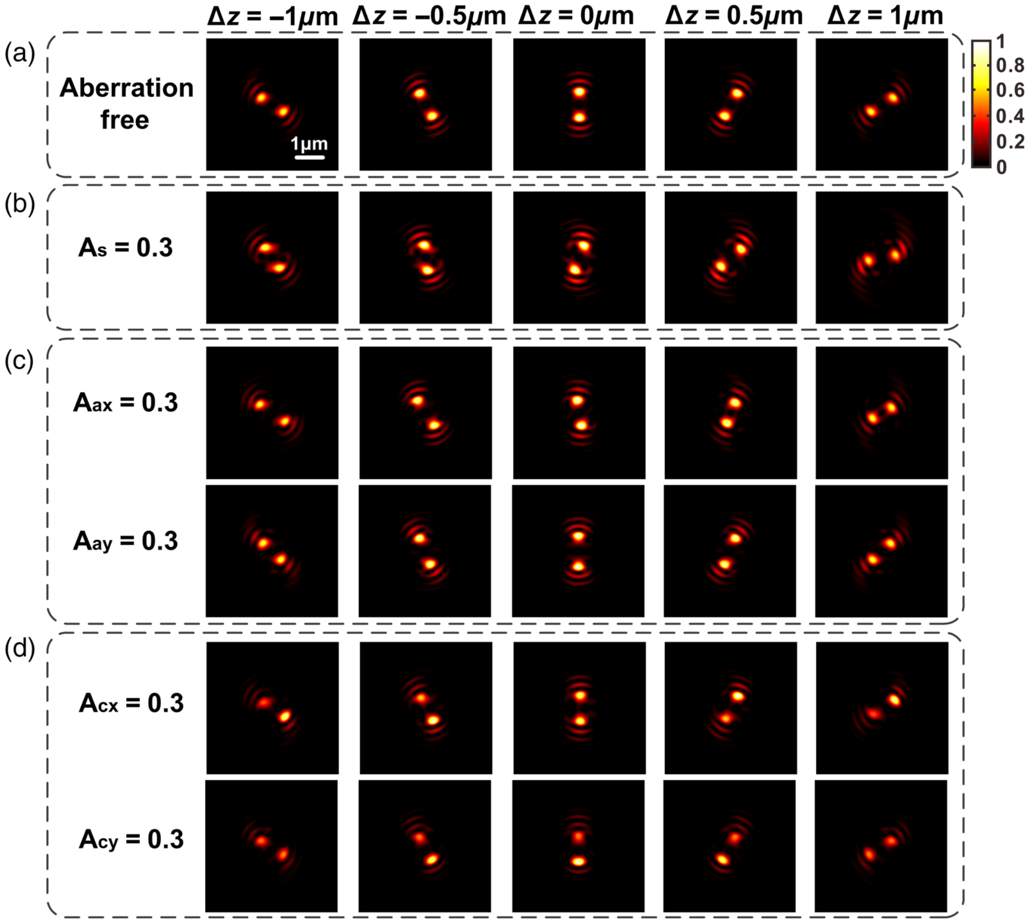

Fig. 1 Calculated intensity distribution of the double-helix PSFs with different types of aberrations. (a) Aberration-free double-helix PSF, (b) double-helix PSF calculated with spherical aberration, (c) double-helix PSFs calculated with 0-deg astigmatism and 45-deg astigmatism, respectively, (d) double-helix PSFs calculated with *x*-coma and *y*-coma, respectively. Coefficients of the aberrations are all set as 0.3λ. $\lambda = 515$ nm, NA $= 1.25$.

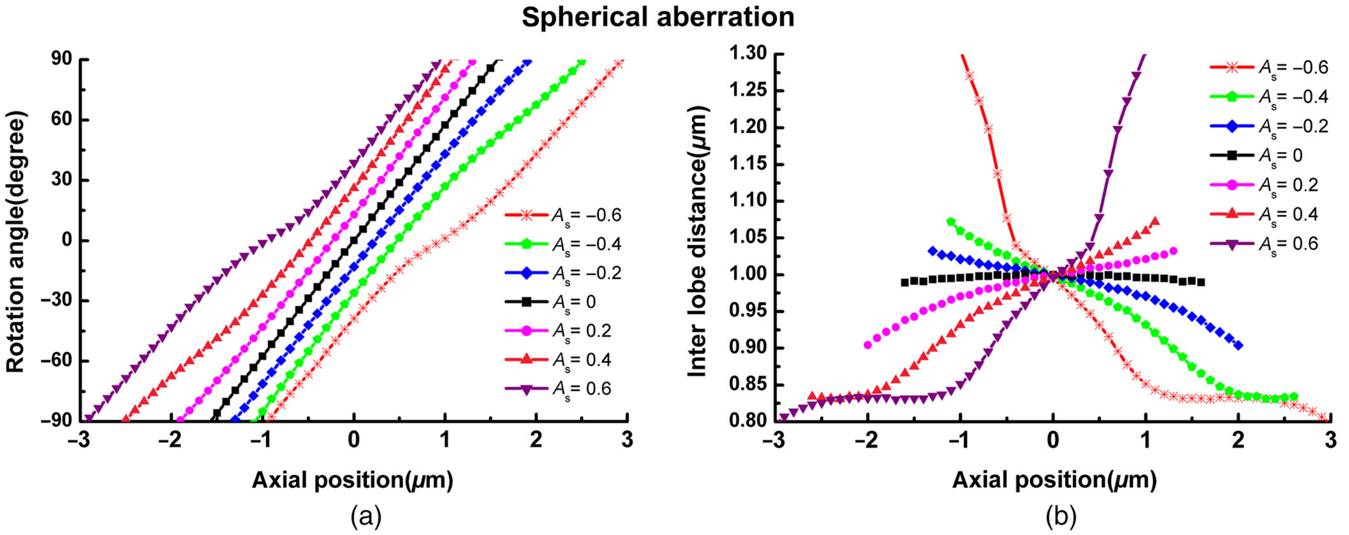

(a)

(b)

Fig. 2 Quantitative deformations of the double-helix PSF ($N = 6$) with varying spherical aberrations. (a) Rotation angle with varying amounts of defocus. (b) Interlobe distance with varying amounts of defocus. The coefficients of spherical aberration vary from −0.6 to 0.6λ.

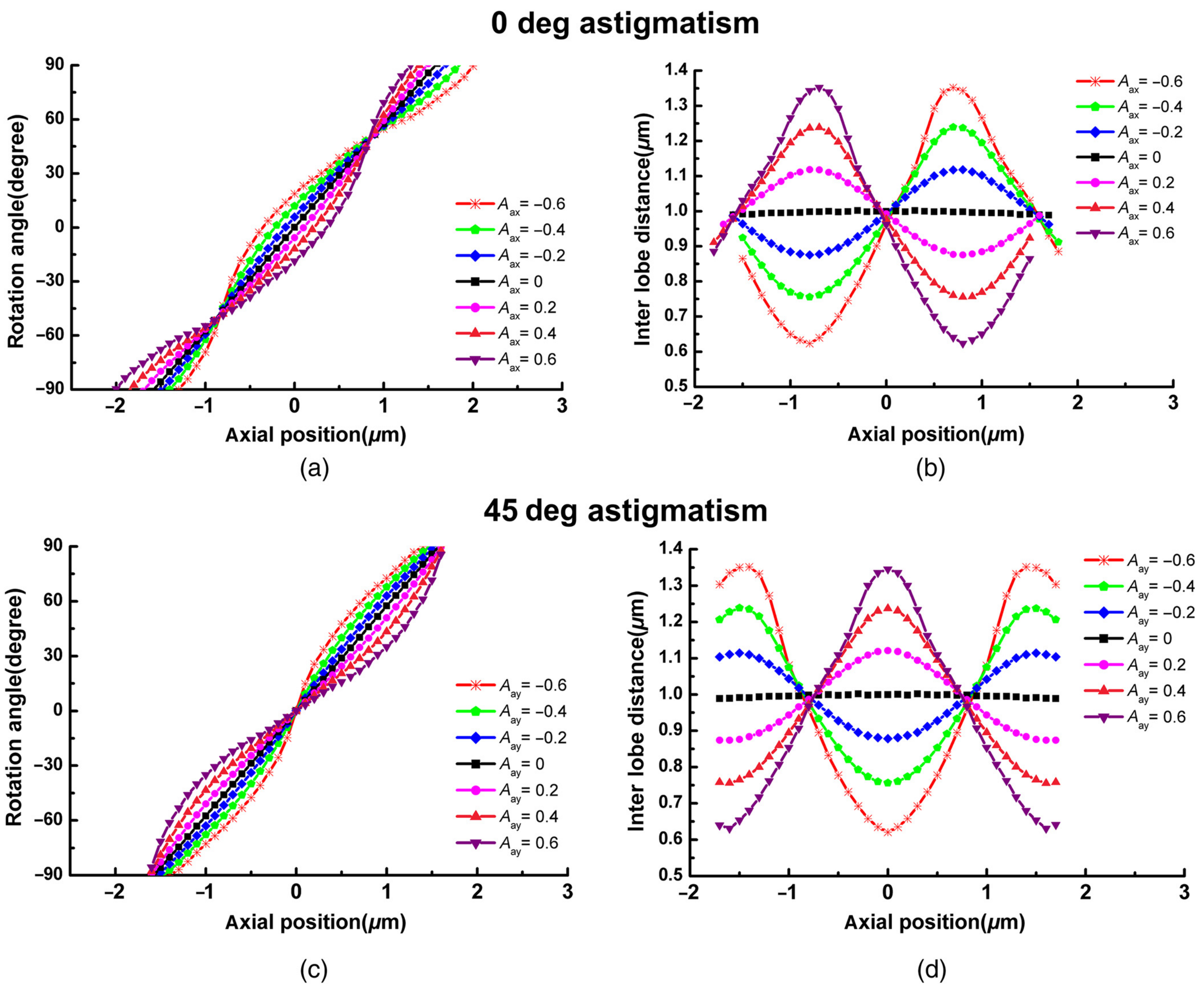

Fig. 3 Quantitative deformations of the double-helix PSF ($N = 6$) with varying 0-deg astigmatism and 45-deg astigmatism. (a) Rotation angle with varying amounts of defocus for 0-deg astigmatism, (b) interlobe distance with varying amounts of defocus for 0-deg astigmatism, (c) rotation angle with varying amounts of defocus for 45-deg astigmatism, and (d) interlobe distance with varying amounts of defocus for 45-deg astigmatism. Both the coefficients of 0-deg astigmatism and the 45-deg astigmatism vary from −0.6 to 0.6λ.

deviates from the original linear curve while keeping constant at two symmetric positions. The difference of the deviated curve from the linear curve can be approximated to a cosine function. The interlobe distance gradually turns nonuniform and the variation resembles a sinusoidal function, whose amplitude increases monotonously with the increasing coefficient.

A similar conclusion can be drawn for 45-deg astigmatism. The constant point of the rotation rate curve turns to the focal plane, which implies the focal plane does not shift with increasing 45-deg astigmatism. The deviation of the rotation rate from the linear curve becomes a sinusoidal function, while the interlobe distance resembles a cosine function.

Figure 4 shows how coma affects the shape of the double-helix PSF. As shown in Figs. 4(a) and 4(c), neither the x-coma nor the y-coma impacts the uniformity of the rotation rate. In fact, not only the rotation rate, but also the interlobe distance is almost unaffected by coma. The interlobe distance curves are not provided here for brevity. Then, only the energy unbalance of the main lobes is involved for the increasing coma [Fig. 1(d)]. To describe the extent of unbalance, we define a specific parameter that is calculated by the natural logarithm value of the lobe-contrast (LVC), as depicted by the following equation:

$$\mathrm{LVC} = \ln\left(\frac{E_1}{E_2}\right), \tag{5}$$

where E_1 and E_2, respectively, denote the energy of two main lobes, which are calculated by integrating the intensity of the corresponding main lobe in the region where the intensity is brighter than half the maximal intensity of the lobe. The LVC curves of x-coma and y-coma are, respectively, shown in Figs. 4(b) and 4(d), which can be approximated to sinusoidal curves and cosinoidal curves. The amplitudes of both curves increase with the absolute value of the coefficients A_{cx} and A_{cy}, respectively.

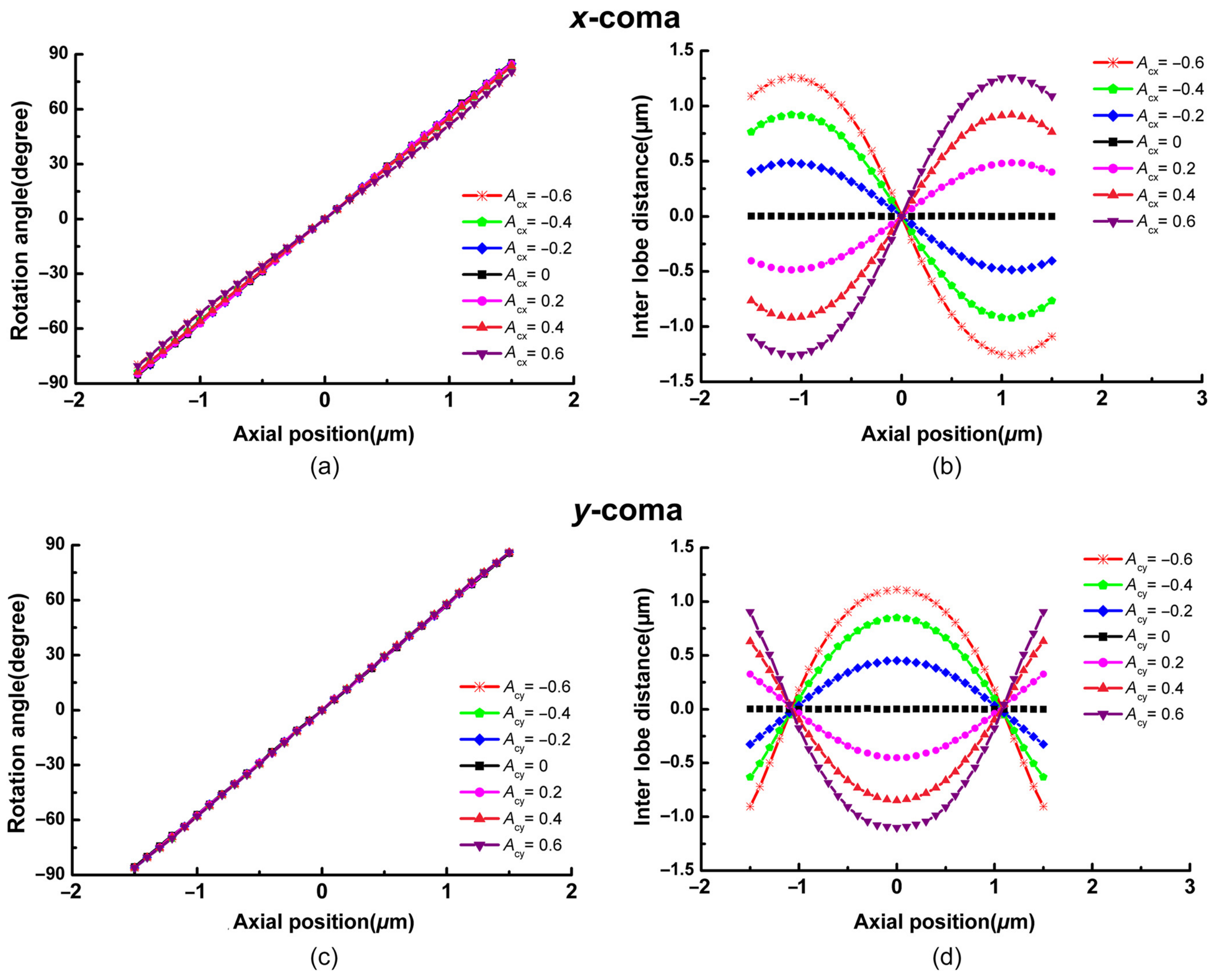

(a) (b) (c) (d)

Fig. 4 Quantitative deformations of the double-helix PSF ($N = 6$) with varying *x*-coma and *y*-coma. (a) Rotation angle with varying amounts of defocus for *x*-coma, (b) interlobe distance with varying amounts of defocus for *x*-coma, (c) rotation angle with varying amounts of defocus for *y*-coma, and (d) interlobe distance with varying amounts of defocus for *y*-coma. Both the coefficients of *x*-coma and the *y*-coma vary from −0.6 to 0.6λ.

2.2 *Correction Methods*

2.2.1 *Single aberration correction*

Based on the analysis above, straightforward correction can be readily carried out if the system only contains a single aberration. As shown in Fig. 2, the difference in the interlobe distance where the rotation angle reaches −90 deg and 90 deg monotonously increases with the increasing spherical aberration. Therefore, with premeasured mapping relation between the difference and the spherical aberration, the coefficient of the spherical aberration can be directly measured by subtracting the interlobe distances at the both ends.

Correction of astigmatism and coma is a bit more complicated, for both of them consist of two components. As mentioned above, the interlobe distance curves of 0-deg astigmatism and 45-deg astigmatism, respectively, resemble a sinusoidal function and a cosinoidal function with identical period. Only when the aberration of the system consists of either 0-deg astigmatism or 45-deg astigmatism can it be directly calculated by measuring the amplitude of the sinusoidal or cosinoidal function. Otherwise, the crosstalk between 0-deg astigmatism and 45-deg astigmatism needs to be considered. To investigate this issue, we simulate the combined effect of the two astigmatisms, as is shown in Fig. 5(a). No distinct crosstalk is found, i.e., the combined effect of the 0-deg astigmatism and the 45-deg astigmatism on the interlobe distance is approximate to the superposition of a sine function and a cosinoidal function with corresponding amplitudes. In other words, the mathematical relation of the combined effect can be described as the following equation:

$$\begin{aligned} f(z) &= C_x \sin(pz) + C_y \cos(pz) \\ &= \sqrt{C_x^2 + C_y^2} \sin\left[pz + \arctan\left(\frac{C_y}{C_x}\right)\right], \end{aligned} \tag{6}$$

where p represents the period of the periodic interlobe distance. C_x and C_y, respectively, denote the weights of the 0-deg astigmatism and the 45-deg astigmatism, which are to be measured.

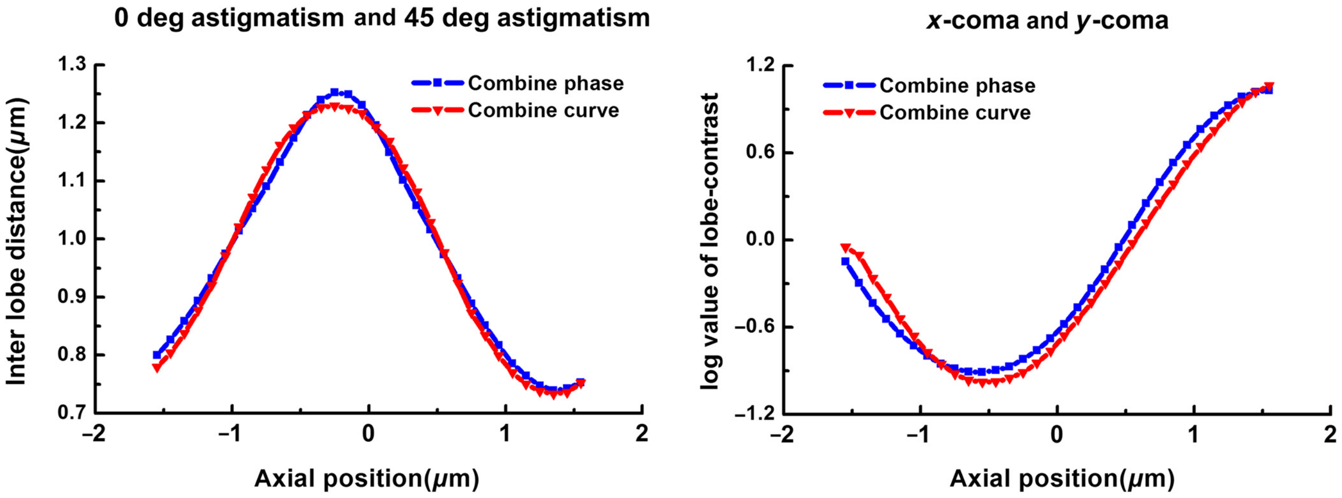

(a) (b)

Fig. 5 Simulative results to verify the absence of the crosstalk between the astigmatism/coma in two directions. (a) The interlobe distance curves to investigate the crosstalk effect between 0-deg astigmatism and 45-deg astigmatism. The blue curve is measured with the double-helix PSF calculated by the combination of the astigmatism in two directions ($A_{\mathrm{ax}} = 0.3\lambda$, $A_{\mathrm{ay}} = 0.3\lambda$), while the red curve is calculated by averaging the curve with the coefficient $A_{\mathrm{ax}} = 0.3\lambda$ and $A_{\mathrm{ay}} = 0.3\lambda$ [see Figs. 3(b) and 3(d)]. (b) The LVC curves to investigate the crosstalk effect between x-coma and y-coma. The blue curve is measured with the double-helix PSF calculated by the combination of the coma in two directions ($A_{\mathrm{cx}} = 0.3\lambda$, $A_{\mathrm{cy}} = 0.3\lambda$), whereas the red curve is calculated by averaging the curve with the coefficient $A_{\mathrm{cx}} = 0.3\lambda$ and $A_{\mathrm{cy}} = 0.3\lambda$ [see Figs. 4(b) and 4(d)].

By experimentally measuring the interlobe distance curve of the aberrated double-helix PSF, the weights C_{x} and C_{y} can be directly calculated. Further, the coefficient of the 0-deg astigmatism and the 45-deg astigmatism can be obtained according to the premeasured mapping relations.

For x-coma and y-coma, the LVC curves are also approximated to a sinusoidal and a cosinoidal function with identical period, respectively. The combined effect of the coma in two directions is also investigated [see Fig. 5(b)], verifying the absence of the crosstalk between the coma in two directions. Therefore, the coefficients of x-coma and y-coma can be measured in a similar approach to astigmatism, and the mathematical relation in Eq. (6) is also applicable for coma.

2.2.2 *Multiple aberration correction*

As demonstrated above, three shape parameters of the double-helix PSF, i.e., rotation rate, interlobe distance, and LVC, are significantly influenced by the aberrations. In turn, the variations of these parameters can provide clues for the determination of the aberration coefficients. Both of the former two are influenced by spherical aberration and astigmatism, while the LVC is only affected by coma. However, as shown in Figs. 2–4, variation in the rotation rate is not as remarkable and regular as the latter two. Thus, in the workflow below, we only use the interlobe distance to determine the spherical aberration and astigmatism. The flowchart of the aberration correction is shown in Fig. 6. The entire process includes three procedures and each procedure corrects one type of aberration. At the beginning of each procedure, the double-helix PSF is experimentally remeasured to minimize the disturbance among different types of aberrations.

Spherical aberration is corrected first. From the above interlobe distance curve in Figs. 2(b), 3(b), and 3(d), we found the discrepancy of the interlobe distance where the rotation angle equals −90 deg and 90 deg only varies with spherical aberration and increases monotonously with the coefficient A_{s}. Thus, spherical aberration can be evaluated by remapping the measured difference to a premeasured lookup table. It is worth noting that only the axial points at both ends are used in this step, which means the measurement speed can be improved by capturing fewer images. Correction of astigmatism follows after the spherical aberration is corrected. The combined effect of the 0-deg astigmatism and the 45-deg astigmatism on the interlobe distance has been investigated in Sec. 2.2.1, which is essentially the overlay of a sine function and a cosine function with different amplitudes, as described in Eq. (6). Thus, the weights of each aberration C_{x} and C_{y} could be obtained with the remeasured interlobe distance curve. By remapping the weights to the simulative results, the coefficients of the 0-deg astigmatism and the 45-deg astigmatism are directly obtained. Similarly, coefficients of x-coma and y-coma can be acquired with the remeasured LVC curve.

3 Experimental Results and Discussion

As a demonstration, correction of the primary aberrations is carried out in an SLM-based adaptive fluorescence microscope, which is shown in Fig. 7. The 3-D PSF of the system is measured by axially scanning a commercial fluorescent nanoparticle with a diameter of 100 nm (F8803, Thermo Fisher Scientific Inc.) through the interested range, which is illuminated by the collimated beam from a solid-state laser ($\lambda = 491$ nm, Calypso 491, Cobolt AB Inc., Sweden). The emission light is collected by the identical microscopy objective (100×, NA = 1.25, Nikon Inc., Japan), of which the back focal plane is reimaged onto the SLM (1920 × 1080 pixels, Pluto II, HoloEye Photonics AG, Germany) with 1:1. The modulated light is then filtered by a long-pass emission filter ($\lambda_c = 500$ nm, Thorlabs Inc.) and collected by the zoom lens, and the specimen is eventually

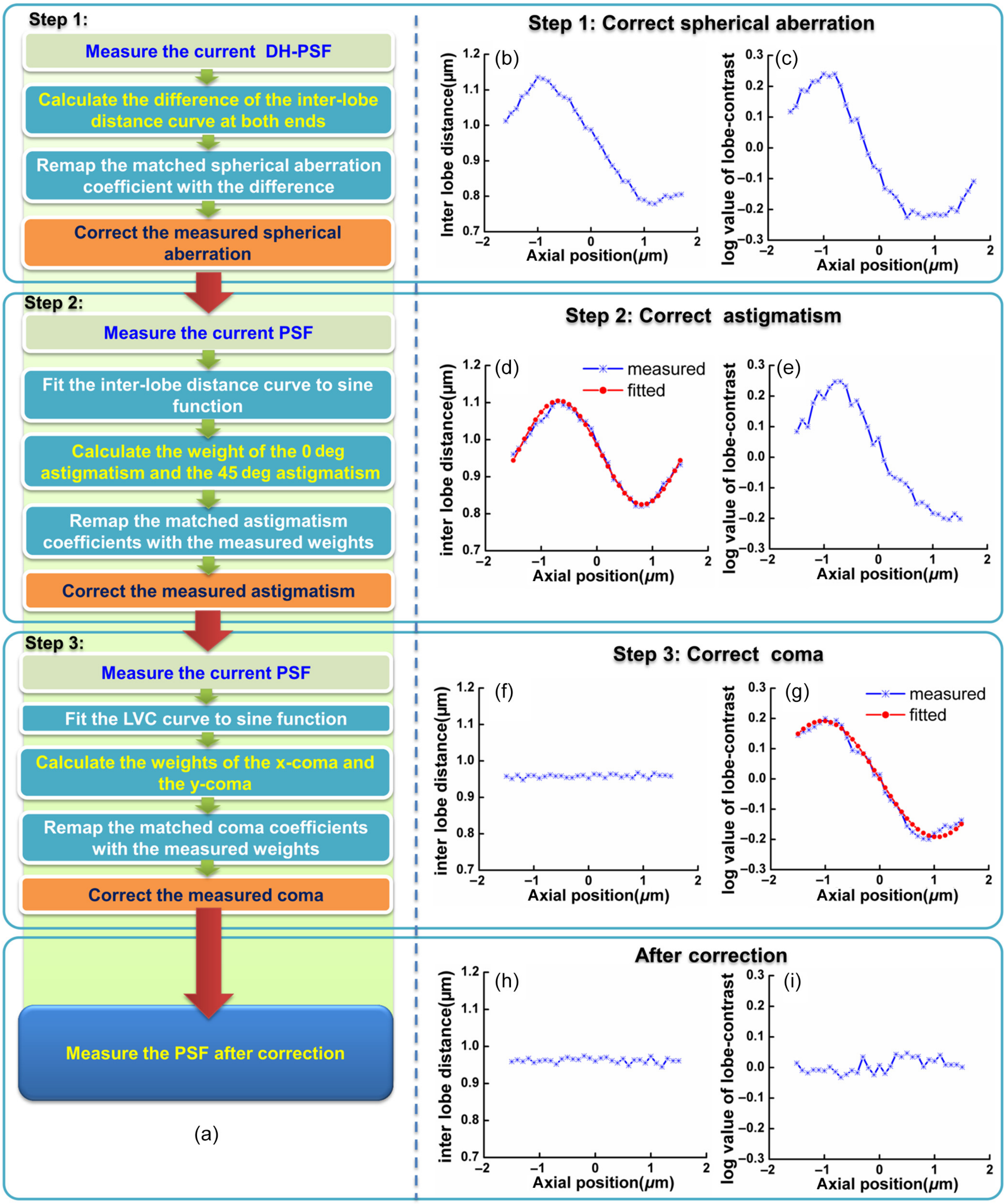

Fig. 6 Flowchart of the aberration correction procedure. (a) The flowchart to clarify the correction process. The entire process includes three steps and each step corrects one type of aberration among spherical aberration, astigmatism, and coma. (b)–(i) The corresponding curves of the experimentally measured PSFs during the correction process for the optical system described in Fig. 7. (b)–(c) are the curves of the initially measured PSF while (d)–(e), (f)–(g), and (h)–(i) are, respectively, measured after each of the three steps. Both of the measured curves in (d) and (g) are fitted with sinusoidal functions with specific periods, the results of which are presented with red lines. The correction time for the whole procedure is about 4 s, which is carried out by a PC (Intel Core i5-4570 CPU @3.2 GHz and 8 GB RAM) with MATLAB.

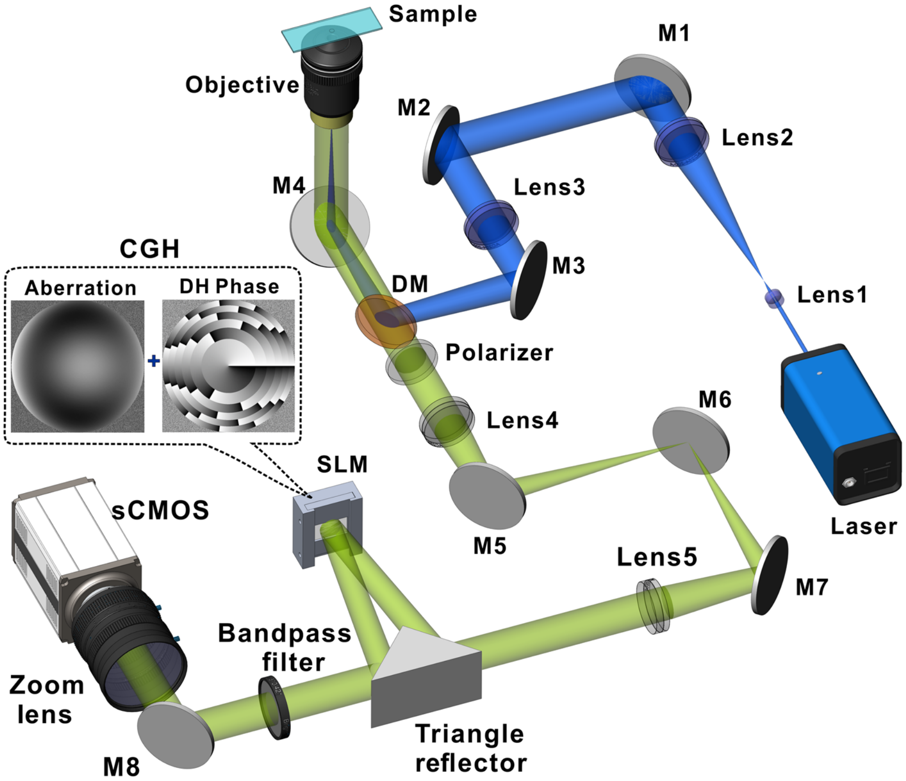

Fig. 7 Schematic diagram of an SLM-based adaptive fluorescence microscope. The expanded and collimated laser beam is projected in parallel onto the specimen as an epi-illumination source. The point spread function of the imaging system is modulated by a phase-only SLM, which also acts as the aberration correction element. The annotated inset implies the CGH loaded on the SLM is calculated by summing the measured conjugate phase-error and the double-helix phase. Finally, the emission light from the specimen is imaged onto a scientific CMOS camera. (DM, dichroic mirror; SLM, spatial light modulator; and M1 to M8: mirrors.)

imaged onto a scientific CMOS camera (Orca Flash4.0, 2048×2048 pixels, 16bits, Hamamatsu Inc., Japan). The double-helix PSF is generated by addressing the corresponding CGH ($N = 6$) on the liquid-crystal panel. Meanwhile, the measured aberrations are compensated by the conjugate phase-error onto the CGH. The axial scanning interval to capture the double-helix PSF is set as 100 nm.

Even though the optical components are elaborately calibrated, primary aberrations including spherical aberration, astigmatism, and coma can be observed by the measured curves in Figs. 6(b) and 6(c), respectively. These aberrations will be corrected in sequence with the developed method. First, the spherical aberration coefficient is easily measured as -0.4λ by calculating the difference of the interlobe distance at both ends of the curve in Fig. 6(b). The spherical aberration can be directly corrected by appending the measured conjugate phase-error on the CGH. The effect of the correction proved to be fairly good by Fig. 6(d), in which the remeasured difference value of the interlobe distance at both ends is close to zero. With the identical interlobe distance curve [Fig. 6(d)], weights of the 0-deg astigmatism or 45-deg astigmatism can be, respectively, measured by fitting the measured curve to sinusoidal function. A_{ax} and A_{ay} are, respectively, calculated as 0 and 0.25λ by remapping the calculated weights to the coefficients. As a consequence, the interlobe distance curve of the PSF after correction becomes uniform as is shown in Fig. 6(f), indicating the astigmatism is well corrected. Similarly, the coma coefficients A_{ax} and A_{ay} are, respectively, measured as -0.08 and 0λ by fitting the measured LVC curve in Fig. 6(g). In the end, after all the primary aberrations are corrected, both the interlobe distance and the LVC turn out to be approximately uniform, which matches with that of the simulated aberration-free double-helix PSF. In total, the aberration of this system mainly consists of -0.4λ spherical aberration, 0.25λ 45-deg astigmatism, and -0.08λ x-coma. The spherical aberration is mostly caused by the refractive-index mismatch of the immersion medium, whereas the astigmatism and the coma collectively stem from the misalignment of the system and the surface curvature of the SLM's reflective panel.

The above correction process takes about 4 s, which mostly consists of the acquisition time of the double-helix PSFs and the computing time of the employed curves. As the total number of acquired images is 64 (two for the first step; 31 for the second step, and the third step), the total acquisition time for the correction sums up to be 3.2 s with a exposure time of 50 ms. With an illumination power of 10 mW, the maximal grayscale level of the acquired double-helix PSF at the focal plane is about 3000 (full gray level is 65,535 with the sCMOS), which is adequate for our correction process. Further reduction in the acquisition time can be achieved by lowering the exposure time of the camera and the axial sampling rate of the PSF. In addition, it also takes about 0.8 s to calculate and fit the interlobe distance curve and the LVC curve in the second and the third step, respectively.

To confirm the validity of the correction, the 3-D Gaussian PSFs before and after correction are measured, as shown in

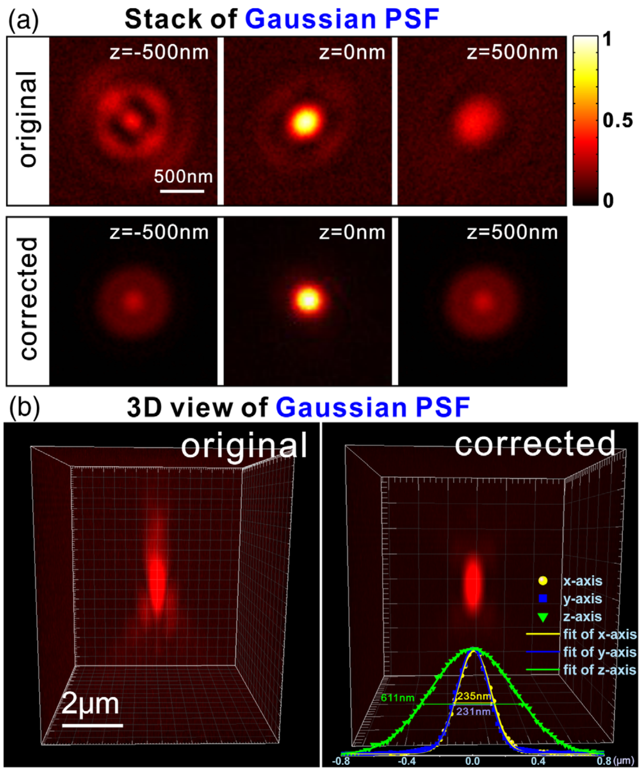

Fig. 8 Measured Gaussian PSF to confirm the validity of the developed approach. (a) Intensity distribution of Gaussian PSF at different axial positions before (top) and after (bottom) correction. (b) Rendered 3-D view of the Gaussian PSFs in (a). The intensity distributions of the corrected PSF along the coordinate axes (*x*, *y*, and *z*) are plotted and fitted with Gaussian functions, as illustrated at the bottom of the corrected PSF. The *x*-, *y*-, and *z*-FWHM are, respectively, measured as 235, 231, and 611 nm.

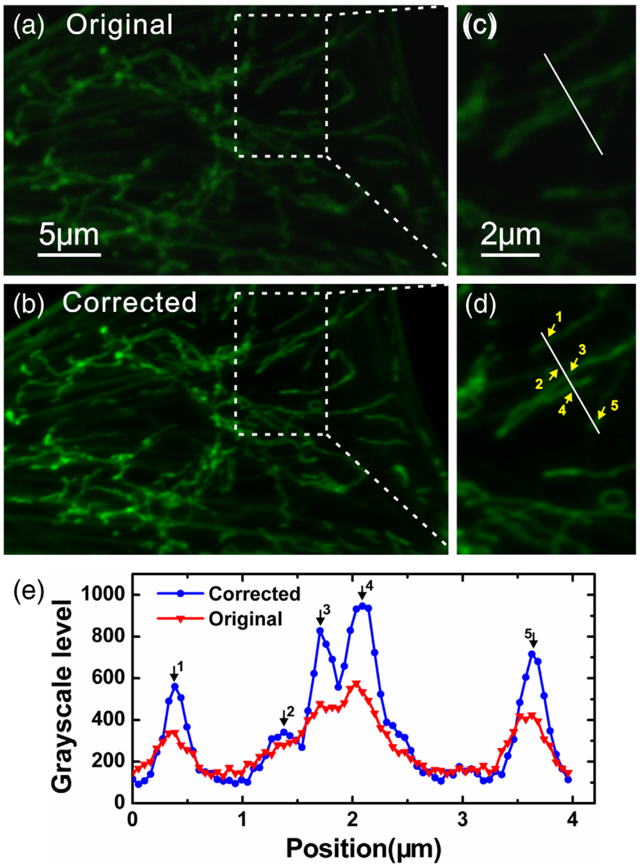

Fig. 9 Image brightness and contrast after the aberration correction are greatly improved, which is verified by the observation results of muntjac skin fibroblast cells. (a) The image captured before the aberration correction, while (b) is the image captured after correction. Both images are acquired with identical illumination intensity and exposure time. (c) and (d) are, respectively, the magnified views of the dashed regions of interest in (a) and (b). Intensity profiles along the solid lines indicated in (c) and (d) are plotted in (e). The peaks marked by the arrows in (e) correspond to the arrow-marked filaments in (d).

Fig. 8(a). Three axial positions are provided here. The slight asymmetry of the defocused spots implies the subtle astigmatism and coma of the system, while significant asymmetry below and above the focal plane reveals the severe spherical aberration. As expected, the symmetry of the PSF greatly improves after the correction, verifying the good performance of the correction method. To provide a more intuitional comparison, the rendered 3-D view of the PSF is shown in Fig. 8(b). In summary, the primary aberrations of the system are properly corrected with the developed method.

Next, a section of muntjac skin fibroblast cells (F36925, Thermo Fisher Scientific Inc.) is tested with epi-illumination in the identical system. The prominent F-actin and mitochondria of the cell are, respectively, labeled with Alexa Fluor 488 phalloidin and an anti-OxPhos Complex V inhibitor protein mouse monoclonal antibody in conjunction with Alexa Fluor 555 goat antimouse IgG. Both of them are excited by the laser and eventually imaged by the camera. Improvement in the image brightness after correction can be instinctively observed by comparing the observation results in Figs. 9(a) and 9(b), respectively. To provide a clearer comparison, magnified views of the two images are also shown in Figs. 9(c) and 9(d). The mitochondria after correction are clearly discernible, while that in the original image remains dark and blurry. The intensity profiles along the solid lines in Figs. 9(c) and 9(d) are shown in Fig. 9(e) to make a quantified comparison of the image quality, in which the brightness of the image is calculated to be improved by a factor of 1.8. Owning to the degraded signal-to-noise rate (SNR) and the distorted PSF, only three of the five marked peaks are recognizable in the original image, while all of them are clear and sharp after correction. Collectively, brightness and contrast of the acquired image are significantly improved after the correction procedure.

It is not difficult to notice the irregular fluctuations in the curves of Fig. 6, which inevitably impacts the measurement precision. Such fluctuations are mainly attributed to the random noise in the measured PSFs that are captured in low light dose. For the fluorescent beads in our experiment, improving the illumination power will be helpful at the very start, but the subsequent images will suffer from poorer SNR because of the increasing photobleaching effect. Thus, the more effective approach to improve the signal level may be to adopt the brighter and antifade subresolution point source, such as quantum dots. In addition, as the difference value used in the first step is calculated by the data at only two points, the measured coefficient of spherical aberration will be more susceptible to the noise. Thus, it is possible to improve the performance of the correction by conducting a second run of the first step in some experiments.

4 Summary

We have quantitatively studied the response of the double-helix PSF to different aberrations. Both the spherical aberration and the astigmatism lead to the nonuniform rotation rate and interlobe distance, while the coma aberration only unbalances the energy of the main lobes. Crosstalk between different aberrations is also investigated, based on which we develop an aberration correction method. Superior to the routine iteration-based correction methods, this approach is iteration-free and the aberration coefficient can be directly calculated with the measured parameter, which is time-saving and takes no convergence risk. The validity of the promoted approach is verified by examining the 3-D Gaussian PSF after correction, which matches pretty well with the well-known aberration-free intensity distribution. The developed approach might provide an easy and economical tool to improve the performance in PSF engineering systems equipped with an SLM.

Disclosures

The authors have no relevant financial interests in this article and no potential conflicts of interest to disclose.

Acknowledgments

This research was supported by the National Key Research and Development Program of China (2017YFC0110100), and the Natural Science Foundation of China (61522511, 91750106, and 81427802).

References

1. S. Quirin, S. R. P. Pavani, and R. Piestun, "Optimal 3D single-molecule localization for superresolution microscopy with aberrations and engineered point spread functions," *Proc. Natl. Acad. Sci. U.S.A.* **109**(3), 675–679 (2012).
2. D. B. Conkey et al., "Three-dimensional parallel particle manipulation and tracking by integrating holographic optical tweezers and engineered point spread functions," *Opt. Express* **19**(5), 3835–3842 (2011).
3. P. Zammit, A. R. Harvey, and G. Carles, "Extended depth-of-field imaging and ranging in a snapshot," *Optica* **1**(4), 209–216 (2014).
4. R. N. Zahreddine, R. H. Cormack, and C. J. Cogswell, "Simultaneous quantitative depth mapping and extended depth of field for 4D microscopy through PSF engineering," *Proc. SPIE* **8227**, 822705 (2012).
5. M. Badieirostami et al., "Three-dimensional localization precision of the double-helix point spread function versus astigmatism and biplane," *Appl. Phys. Lett.* **97**(16), 161103 (2010).
6. C. Snoeyink and S. Wereley, "Single-image far-field subdiffraction limit imaging with axicon," *Opt. Lett.* **38**(5), 625–627 (2013).
7. O. E. Olarte et al., "Decoupled illumination detection in light sheet microscopy for fast volumetric imaging," *Optica* **2**(8), 702–705 (2015).
8. S. Quirin, D. S. Peterka, and R. Yuste, "Instantaneous three-dimensional sensing using spatial light modulator illumination with extended depth of field imaging," *Opt. Express* **21**(13), 16007–16021 (2013).
9. B. Huang et al., "Three-dimensional super-resolution imaging by stochastic optical reconstruction microscopy," *Science* **319**(5864), 810–813 (2008).
10. S. Quirin and R. Piestun, "Depth estimation and image recovery using broadband, incoherent illumination with engineered point spread functions [Invited]," *Appl. Opt.* **52**(1), A367–A376 (2013).
11. R. Piestun, Y. Y. Schechner, and J. Shamir, "Propagation-invariant wave fields with finite energy," *J. Opt. Soc. Am. A* **17**(2), 294–303 (2000).
12. S. Abrahamsson et al., "Fast multicolor 3D imaging using aberration-corrected multifocus microscopy," *Nat. Methods* **10**(1), 60–63 (2013).
13. P. Kner et al., "High-resolution wide-field microscopy with adaptive optics for spherical aberration correction and motionless focusing," *J. Microsc.* **237**(2), 136–147 (2010).
14. N. Matsumoto et al., "Correction of depth-induced spherical aberration for deep observation using two-photon excitation fluorescence microscopy with spatial light modulator," *Biomed. Opt. Express* **6**(7), 2575–2587 (2015).
15. C. Sheppard and T. Wilson, "Effect of spherical aberration on the imaging properties of scanning optical microscopes," *Appl. Opt.* **18**(7), 1058–1063 (1979).
16. M. J. Booth, "Adaptive optical microscopy: the ongoing quest for a perfect image," *Light Sci. Appl.* **3**(4), e165 (2014).
17. N. Ji, "Adaptive optical fluorescence microscopy," *Nat. Methods* **14**(4), 374–380 (2017).
18. O. Azucena et al., "Wavefront aberration measurements and corrections through thick tissue using fluorescent microsphere reference beacons," *Opt. Express* **18**(16), 17521–17532 (2010).
19. O. Azucena et al., "Adaptive optics wide-field microscopy using direct wavefront sensing," *Opt. Lett.* **36**(6), 825–827 (2011).
20. X. Tao et al., "Adaptive optics confocal microscopy using direct wavefront sensing," *Opt. Lett.* **36**(7), 1062–1064 (2011).
21. M. Rueckel, J. A. Mack-Bucher, and W. Denk, "Adaptive wavefront correction in two-photon microscopy using coherence-gated wavefront sensing," *Proc. Natl. Acad. Sci. U.S.A.* **103**(46), 17137–17142 (2006).
22. B. Hanser et al., "Phase-retrieved pupil functions in wide-field fluorescence microscopy," *J. Microsc.* **216**(1), 32–48 (2004).
23. A. von Diezmann et al., "Correcting field-dependent aberrations with nanoscale accuracy in three-dimensional single-molecule localization microscopy," *Optica* **2**(11), 985–993 (2015).
24. M. J. Booth et al., "Adaptive aberration correction in a confocal microscope," *Proc. Natl. Acad. Sci. U.S.A.* **99**(9), 5788–5792 (2002).
25. D. Débarre et al., "Adaptive optics for structured illumination microscopy," *Opt. Express* **16**(13), 9290–9305 (2008).
26. B. M. Hanser et al., "Phase retrieval for high-numerical-aperture optical systems," *Opt. Lett.* **28**(10), 801–803 (2003).
27. A. Jesacher et al., "Wavefront correction of spatial light modulators using an optical vortex image," *Opt. Express* **15**(9), 5801–5808 (2007).
28. E. H. Waller, M. Renner, and F. G. Von, "Active aberration- and point-spread-function control in direct laser writing," *Opt. Express* **20**(22), 24949–24956 (2012).
29. J. Hering, E. H. Waller, and G. Von Freymann, "Automated aberration correction of arbitrary laser modes in high numerical aperture systems," *Opt. Express* **24**(25), 28500–28508 (2016).
30. M. Siemons et al., "High precision wavefront control in point spread function engineering for single emitter localization," *Opt. Express* **26**(7), 8397–8416 (2018).
31. Z. Wang et al., "Single shot, three-dimensional fluorescence microscopy with a spatially rotating point spread function," *Biomed. Opt. Express* **8**(12), 5493–5506 (2017).
32. M. Baránek and Z. Bouchal, "Optimizing the rotating point spread function by SLM aided spiral phase modulation," *Proc. SPIE* **9441**, 94410N (2014).
33. A. Greengard, Y. Y. Schechner, and R. Piestun, "Depth from diffracted rotation," *Opt. Lett.* **31**(2), 181–183 (2006).
34. S. R. P. Pavani and R. Piestun, "Three dimensional tracking of fluorescent microparticles using a photon-limited double-helix response system," *Opt. Express* **16**(26), 22048–22057 (2008).
35. I. Izeddin et al., "PSF shaping using adaptive optics for three-dimensional single-molecule super-resolution imaging and tracking," *Opt. Express* **20**(5), 4957–4967 (2012).
36. S. Ghosh and C. Preza, "Characterization of a three-dimensional double-helix point-spread function for fluorescence microscopy in the presence of spherical aberration," *J. Biomed. Opt.* **18**(3), 036010 (2013).
37. Z. Cao and K. Wang, "Effects of astigmatism and coma on rotating point spread function," *Appl. Opt.* **53**(31), 7325–7330 (2014).
38. S. Prasad, "Rotating point spread function via pupil-phase engineering," *Opt. Lett.* **38**(4), 585–587 (2013).
39. V. Mahajan, *Optical Imaging and Aberrations, Part III: Wavefront Analysis*, SPIE Press, Bellingham, Washington (2013).

Zhaojun Wang is a PhD candidate at Xi'an Institute of Optics and Precision Mechanics, Chinese Academy of Sciences. He received his BS degree in optical information science and technology at Huazhong University of Science and Technology in 2013. His research focuses on extended depth-of-field imaging and super-resolution optical microcopy.

Yanan Cai is a PhD candidate at Xi'an Institute of Optics and Precision Mechanics, Chinese Academy of Sciences. She received her BS degree in physics at Northeast Forestry University in 2013. Her research focuses on reconstruction of tightly focused vector beams.

Yansheng Liang is a PhD candidate at Xi'an Institute of Optics and Precision Mechanics, Chinese Academy of Sciences. He received his BS degree in physics from Nankai University in 2011. His research focuses on optical micromanipulation and beam shaping.

Dan Dan received his MS degree in physical electronics from the School of Physics and Optoelectronic Engineering, Xidian University in 2010, and his PhD at Xi'an Institute of Optics and Precision Mechanics, Chinese Academy of Sciences in 2017. Currently, he is an associate professor at the State Key Laboratory of Transient Optics and Photonics, Xi'an Institute of Optics and Precision Mechanics, Chinese Academy of Sciences. His research is focused on structured illumination microscopy for super-resolution and optical sectioning.

Baoli Yao obtained his PhD in optics from Xi'an Institute of Optics and Precision Mechanics, Chinese Academy of Sciences in 1997, and pursued his postdoctoral work in the Technical University of Munich, Germany, from 1997 to 1998. Currently, he is associated with the State Key Laboratory of Transient Optics and Photonics, Xi'an Institute of Optics and Precision Mechanics, Chinese Academy of Sciences, and is the deputy director of the lab. His research areas include super-resolution optical microscopy, digital holographic microscopy, optical micromanipulation and microfabrication, optical data storage, and information processing.

Ming Lei received his BE degree at the School of Physics and Optoelectronic Engineering, Xidian University in 2000, and his PhD at Xi'an Institute of Optics and Precision Mechanics, Chinese Academy of Sciences in 2007. He was trained as a postdoctoral research fellow in the Department of Chemistry, University of Konstanz, Germany, from 2008 to 2010. Currently, he is a professor at the State Key Laboratory of Transient Optics and Photonics, Xi'an Institute of Optics and Precision Mechanics, Chinese Academy of Sciences. His research is focused on super-resolution microscopy and optical trapping technologies.